Two-dimensional liquid crystalline growth within a phase-field-crystal model

Sai Tang,[1,2] Simon Praetorius,[2] Rainer Backofen,[2] Axel Voigt,[2,3,*] Yan-Mei Yu,[4] and Jincheng Wang[1]

[1]*State Key Laboratory of Solidification Processing, Northwestern Polytechnical University, Youyi Western Road 127, 710072 Xi'an, China*

[2]*Institut für Wissenschaftliches Rechnen, Technische Universität Dresden, 01062 Dresden, Germany*

[3]*Center of Advanced Modeling and Simulations, Technische Universität Dresden, 01062 Dresden, Germany*

[4]*Institute of Physics, Chinese Academy of Science, P.O. Box 603, 100190 Beijing, China*

(Received 8 January 2015; published 10 July 2015)

By using a two-dimensional phase-field-crystal (PFC) model, the liquid crystalline growth of the plastic triangular phase is simulated with emphasis on crystal shape and topological defect formation. The equilibrium shape of a plastic triangular crystal (PTC) grown from an isotropic phase is compared with that grown from a columnar or smectic-*A* (CSA) phase. While the shape of a PTC nucleus in the isotropic phase is almost identical to that of the classical PFC model, the shape of a PTC nucleus in CSA is affected by the orientation of stripes in the CSA phase, and irregular hexagonal, elliptical, octagonal, and rectangular shapes are obtained. Concerning the dynamics of the growth process, we analyze the topological structure of the nematic order, which starts from nucleation of $+\frac{1}{2}$ and $-\frac{1}{2}$ disclination pairs at the PTC growth front and evolves into hexagonal cells consisting of $+1$ vortices surrounded by six satellite $-\frac{1}{2}$ disclinations. It is found that the orientational and the positional order do not evolve simultaneously; the orientational order evolves behind the positional order, leading to a large transition zone, which can span over several lattice spacings.

DOI: 10.1103/PhysRevE.92.012504 PACS number(s): 61.30.Dk, 68.08.De, 64.70.dm, 82.70.Dd

I. INTRODUCTION

Liquid crystals consist of particles that possess both a translational and an orientational degree of freedom. In contrast to spherical particles, which, in general, exhibit only pure fluid or crystalline bulk phases, the additional orientational degree of freedom in liquid crystals induces a wealth of "mesophases" with partial orientational and translational (or positional) ordering [1,2]. Apart from the dilute disordered state, there is a nematic phase which is orientationally ordered but translationally disordered, and there is a plastic crystal which is positionally ordered but orientationally disordered, although its orientational disorder is only global and not local [3]. Then there are columnar and smectic phases which are positionally ordered in fewer directions than the full translational space and are orientationally ordered as well. Finally, the full crystalline state has full positional and both local and global orientational orders. We will here concentrate on the plastic crystal phase (see [4–8] for earlier research), which in two dimensions is termed a plastic triangular crystal (PTC) and has been considered in [9–12], and we concentrate on growth shapes and topological defect formation. Topological defects in two-dimensional structures are well studied (see [13] and [10] and the references therein for orientational and positional ordering, respectively). However, the interplay of orientational and positional ordering as it occurs during the self-assembly of PTC out of other phases remains unclear. We here address this interplay using a phase-field-crystal (PFC) model by analyzing the growth of PTC from an isotropic and a columnar or smectic-*A* (CSA) phase.

PFC models, introduced by Elder *et al.* [14,15], are today widely used in modeling crystallization (e.g., [16–20]). As a mean-field approach, the PFC model is capable of describing, over diffusive time scales, atomic arrangements, crystalline defects, and interface structures of the crystal growth process. The modeling approach has also been generalized to other systems, e.g., liquid crystals. Liquid crystal PFC (LC-PFC) models for apolar particles [21] are formulated in terms of three order parameter fields [22], including the reduced translational density $\psi(\vec{r},t)$, the local nematic order parameter $S(\vec{r},t)$, and the nematic director $\hat{n}(\vec{r},t)$, wherein $\vec{r}=(x,y)$ and t are position and time, respectively. Even if we consider only two-dimensional systems, the model is formulated for three-dimensional liquid crystals as well (see, e.g., [23]). The couplings among these fields produce the liquid crystalline phases, such as isotropic, nematic, columnar or smectic-*A*, and plastic crystalline phases. Achim *et al.* [24] numerically determined the stable liquid crystalline phases in two spatial dimensions, and Praetorius *et al.* [25] found the corresponding phase coexistence regions for special coupling-parameter combinations. The latter group also explored the structure and width of the equilibrium PTC-isotropic and PTC-CSA interfaces as a function of model parameters related to the coupling strength of the three fields and crystal anisotropy.

We here extend these studies to investigate the growth of a PTC nucleus from the isotropic and the CSA phases. Experimental results [26,27] have shown such growth processes to produce a large variety of shapes, e.g., with smooth or faceted dendrites, faceted equilibrium shapes, or circular shapes. The growth of succinonitrile and pivalic acid [26] from melt, for example, show high similarity to metal systems in terms of the observed morphologies. This suggests that for some plastic materials the coupling strength of the translational and orientational fields may have only limited influence on the morphology. Is this specific to these materials, or can the coupling strength also play an important role in the shape evolution of plastic crystal growth? Besides the morphology we will also consider topological defects of the nematic director $\hat{n}(\vec{r})$. These defects have already been considered, e.g., in [3,24,28,29]. Achim *et al.* [24] obtained vortices, disclinations, sources or sinks, and hyperbolic points

*Corresponding author: axel.voigt@tu-dresden.de

in PTC. Cremer *et al.* [3] depicted the topological defect structure in PTC and proposed a simplified but topologically equivalent model to explain qualitatively how the topological defect structure of hexagonal symmetry arises. Nevertheless, the understanding about the process of topological defect formation is still limited. How does the topological defect originate from the mother phase? How is a topological defect structure of geometric symmetry constructed? We will answer these questions by visualizing the topological defect formation on the particle scale using the LC-PFC model.

II. LIQUID CRYSTAL PFC MODEL

A. Free-energy functional

We consider a formulation of the LC-PFC model using the reduced translational density field $\psi(\vec{r},t)$ and the symmetric and traceless nematic order tensor field $Q(\vec{r},t)$ with the components $Q_{ij}(\vec{r},t)$. In two dimensions the $Q_{ij}(\vec{r},t)$ fields are related to the nematic order parameter $S(\vec{r},t)$ and the nematic director $\hat{n}(\vec{r},t) = (n_1,n_2)$ fields through

$$Q_{ij}(\vec{r},t) = S(\vec{r},t)\left[n_i(\vec{r},t)n_j(\vec{r},t) - \tfrac{1}{2}\delta_{ij}\right]. \tag{1}$$

The dimensionless free-energy functional is written as [22,24,25]

$$\begin{aligned}\mathcal{F}[\psi,Q_{ij}] = \int d^2r \Bigg[&-\frac{\psi^3}{3} + \frac{\psi^4}{6} + (\psi-1)\frac{\psi Q_{kl}^2}{4} \\ &+ \frac{Q_{kl}^2 Q_{mn}^2}{64} + A_1\psi^2 + A_2\psi(\Delta+\Delta^2)\psi \\ &+ B_3(\partial_k\psi)(\partial_l Q_{kl}) + D_1 Q_{kl}^2 + D_2(\partial_l Q_{kl})^2\Bigg],\end{aligned} \tag{2}$$

where Einstein's sum convention is used, $\Delta \equiv \partial_k^2$ is the Laplace operator, and A_1, A_2, B_3, D_1, and D_2 are dimensionless model parameters, with A_1 controlling the crystalline anisotropy [19,30] and B_3 controlling the coupling strength between $\psi(\vec{r},t)$ and $Q_{ij}(\vec{r},t)$.

B. Dynamic equations

The dynamic equations of $\psi(\vec{r},t)$ and $Q_{ij}(\vec{r},t)$ are deduced from classical dynamical density functional theory (DDFT), as written by [31,32]

$$\dot{\psi} + \partial_i J_i^{\psi} = 0, \tag{3}$$

$$\dot{Q}_{ij} + \Phi_{ij}^{Q} = 0, \tag{4}$$

where $J_i^{\psi}(\vec{r},t)$ is the dimensionless current and $\Phi_{ij}^{Q}(\vec{r},t)$ is the dimensionless quasi-current. In the constant-mobility approximation, this current and quasi-current are given by [16]

$$J_i^{\psi} = -2\alpha_1(\partial_i\psi^{\natural}) - 2\alpha_3(\partial_j Q_{ij}^{\natural}), \tag{5}$$

$$\Phi_{ij}^{Q} = -4\alpha_1(\Delta Q_{ij}^{\natural}) - 2\alpha_3[2(\partial_i\partial_j\psi^{\natural}) - \delta_{ij}(\Delta\psi^{\natural})] + 8\alpha_4 Q_{ij}^{\natural}, \tag{6}$$

where α_1, α_3, and α_4 are dimensionless mobilities. The thermodynamic conjugates $\psi^{\natural}$ and $Q_{ij}^{\natural}$ are given by

$$\psi^{\natural} = \frac{\delta\mathcal{F}}{\delta\psi}, \quad Q_{ij}^{\natural} = \frac{\delta\mathcal{F}}{\delta Q_{ij}}, \tag{7}$$

which read

$$\begin{aligned}\psi^{\natural} = &-\psi^2 + \frac{2}{3}\psi^3 + (2\psi-1)\frac{Q_{ij}^2}{4} + 2A_1\psi \\ &+ 2A_2(\Delta+\Delta^2)\psi - B_3(\partial_i\partial_j Q_{ij}),\end{aligned} \tag{8}$$

$$\begin{aligned}Q_{ij}^{\natural} = &\psi(\psi-1)Q_{ij} + \frac{Q_{ij}Q_{kl}^2}{8} \\ &- B_3[2(\partial_i\partial_j\psi) - \delta_{ij}\Delta\psi] + 4D_1 Q_{ij} \\ &- 2D_2\partial_k[\partial_i Q_{kj} + \partial_j Q_{ki} - \delta_{ij}(\partial_l Q_{kl})].\end{aligned} \tag{9}$$

The dynamic equations (3) and (4) will be solved numerically by a semi-implicit Fourier method; see the Appendix for details.

III. RESULTS AND DISCUSSION

We consider first a PTC nucleus in the isotropic and CSA phases and show that the coupling strength B_3 between the nematic order tensor and the density has only a minor influence on the crystal morphology. Second, the ordering of the nematic order tensor during the growth of a PTC into the CSA phase is studied. Independent of the coupling strength B_3, +1 disclinations in the PTC phase are formed by coalescence of two $+\frac{1}{2}$ disclinations. Only the time evolution and the delay of the defect formation with respect to the interface velocity are dependent on B_3.

A. Stationary interfaces

All simulations are carried out with $A_2 = 14$, $D_1 = 1$, and $D_2 = 0.8$. Variations of these parameters turn out to show only minor effects on the considered situation of isotropic, PTC, and CSA phases. We vary the mean density $\bar{\psi}_0$, anisotropy A_1, and coupling strength B_3, which can be used to control the liquid crystal phases [24,25].

In Fig. 1, the phase diagram without coupling to the nematic tensor, $B_3 = 0$, is compared to the phase diagrams with weak and strong coupling, $B_3 = -0.4$ and -1.6, respectively. The structure of the phase diagrams reflects that of the classical PFC, where the PTC and the CSA phases correspond to the crystal and stripe phases (cf. [14]). Thus, analog to the classical PFC, A_1 is connected to the undercooling. The coupling strength does not change the phase diagram qualitatively. Small coupling, $B_3 = -0.4$, shows no influence; only strong coupling, $B_3 = -1.6$, slightly increases the region of a stable PTC phase. Thus, the coexistence region of a PTC-isotropic phase and a PTC-CSA phase is nearly independent of B_3 and allows us to study the interface properties dependent on only coupling strength B_3. In order to minimize boundary effects in our simulations, a single PTC nucleus is considered in the center of the simulation domain. To neglect stresses induced by the boundaries, parameters A_1 and B_3 are varied, and the corresponding $\bar{\psi}_0$ value is chosen carefully to ensure

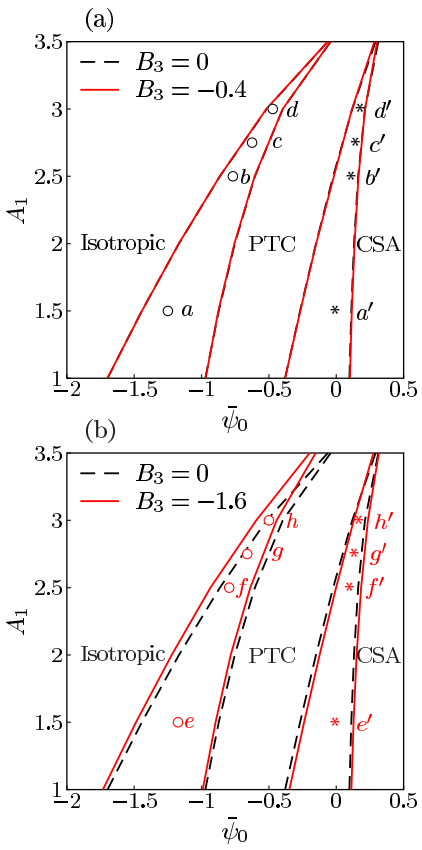

FIG. 1. (Color online) LC-PFC phase diagrams as a function of $\bar{\psi}_0$ and A_1 for $B_3 = 0$, (a) -0.4, and (b) -1.6, which correspond to zero, weak, and strong coupling strength between the density field and the nematic-order field, respectively. The small letters correspond to parameters used in our simulations.

coexistence with the surrounding phase (cf. [25]). As long as we are in the coexistence region of the phase diagram, variations in $\bar{\psi}_0$ do not change the morphology but determine the size of the PTC nucleus. Size dependence for very small nuclei, as observed in [30], can be neglected here as only large enough PTCs are considered. The domain size is at least 2 times bigger than the shown PTC for the coexistence with the CSA phase, and possible size dependencies are regularly checked by enlarging the simulation box and comparing the results.

1. Equilibrium shape of PTC in the isotropic phase

The equilibrium shape of a PTC nucleus in the isotropic phase is simulated for increasing A_1. Simulation results and parameters are summarized in Figs. 2(a)–2(c). For every equilibrium shape the interface has been extracted and normalized by the extension of the PTC nucleus in the [12] direction. Without coupling, $B_3 = 0$, the shape changes from a perfect hexagon, $A_1 = 1.5$, to a circle, $A_1 = 3$. The width of the interface seen in the inlet of Fig. 2(a) widens for increasing A_1. This corresponds to the findings in classical PFC for decreasing undercooling (cf. [30]). Coupling to the nematic tensor does not change the picture at all [see Fig. 2(b)]. The anisotropy of the nucleus is quantified by the reduced aspect ratio α (ratio of the nucleus extension in the [10] and [12] directions). Based on the Wulff construction, the aspect ratio α relates to the anisotropy of the line energy [30,33]. Thus, the nematic order has a minor influence on the anisotropy of the line energy of the PTC phase in the isotropic phase, and the anisotropy is well controlled by only A_1 and reflects the results of classical PFC [30].

2. Crystal shape of PTC in the CSA phase

For PTC growth in the CSA phase, the orientation of the nucleus with respect to the stripes of the CSA phase becomes important. We consider two setups. First, the [12] direction of the PTC is perpendicular to the stripes. That is, closed-packed layers of the crystal and stripes of the CSA phase are aligned perfectly (case I). Second, the crystal is rotated by $\frac{\pi}{2}$, and the stripes do not fit the particle layers (case II).

The simulation results for case I are shown in Figs. 2(d)–2(f). As before, the growth of a small PTC nucleus is simulated until a steady state is reached. The anisotropy of the steady state is again controlled by A_1. Increasing A_1 changes the morphology from faceted to round [Fig. 2(d)]. But here the round shapes are elongated along the stripes, while the faceted shapes are elongated perpendicular to the stripes. Unlike growth into the isotropic phase, the growth kinetics is very anisotropic for small A_1. That is, the growth of the crystal facet in the [12] direction is faster than the growth of the [21] facet. This leads to a smaller [12] facet compared to the [21] facet of the stationary crystal. The ratio of the length of two facets is dependent on the initial condition and domain size of the simulation. Thus, they are just metastable or frozen states and do not represent the overall anisotropy of the interface energy. But, as there are always facets, we can conclude that the line energy has strong minima for the [12] and [21] facets, but we cannot judge the energy ratio between them.

If we increase the coupling strength B_3, the transition from faceted to round shapes does not change, but the elongation of the round shapes along the stripes is slightly increased [see Fig. 2(e)]. The coupling strength in this situation is more important than for the PTC-isotropic interface.

In case II, the crystal is rotated, and the simulations are done as before. The PTC no longer fits into the layers of the CSA phase (see Fig. 3). In this configuration only small crystals for small A_1 can be stabilized. Various attempts to increase nucleus sizes lead to rotating or vanishing crystals. The [10] plane of the PTC is parallel to the stripes and stabilized by the CSA phase. This leads roughly to a hexagon with the edges in the [10]-direction cut [indicated by dashed red lines in Figs. 3(c) and 3(d)]. The CSA phase is also distorted near the interface. If the stripes do not fit the structure of the PTC, the crystal and the CSA phases are inhomogeneously strained. This is clearly shown by the bending of the close-packed particle layers in Fig. 3(b) and the waviness of the stripes in the CSA phase. The coupling strength increases the discussed features and leads to nearly rectangular shapes [Fig. 3(b) and 3(d)]. Thus, case II is energetically penalized by the elastic stress in the crystal induced by the surrounding CSA phase and will most likely not occur in the liquid crystal phase transition. In the following we will concentrate on case I.

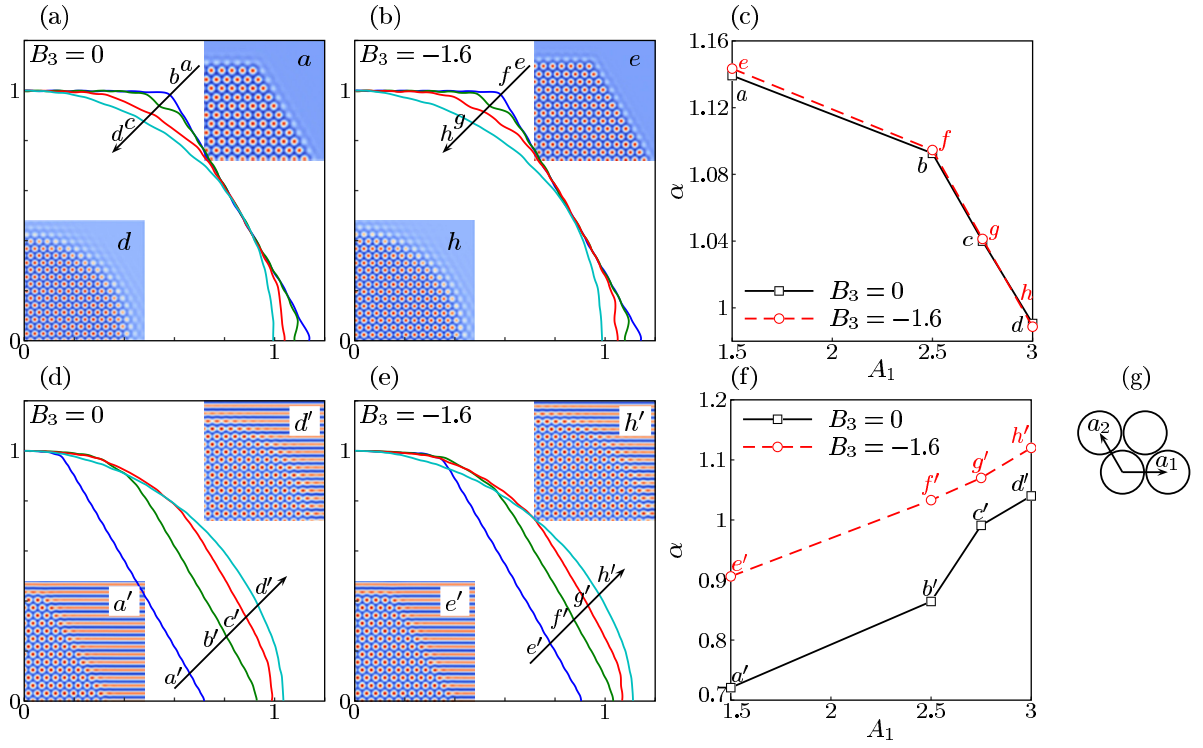

FIG. 2. (Color online) The equilibrium shape of the PTC nucleus in the isotropic phase for (a) $B_3 = 0$ and (b) $B_3 = -1.6$ and (c) the corresponding contour line and aspect ratio α as a function of A_1. The considered examples a-d and e-h correspond to the depicted points in Fig. 1. The insets show the obtained equilibrium shapes for two selected points. (d) and (e) The morphology of a PTC nucleus in a CSA phase for $A_1 = 1.5$, where the close-packed direction of the PTC phase is parallel to the stripe in the CSA phase. (d) shows the equilibrium PTC shapes for $B_3 = 0$ for the considered examples a′-d′, and (e) shows the shapes of growing PTC for $B_3 = -1.6$ for h′-e′, again corresponding to the depicted points in Fig. 1. The insets again show selected growth shapes. (f) The aspect ratio α as a function of A_1 for the equilibrium PTC shape for $B_3 = 0$ and the growing shape for $B_3 = -1.6$. (g) The definition of crystal unit vectors a_1 and a_2.

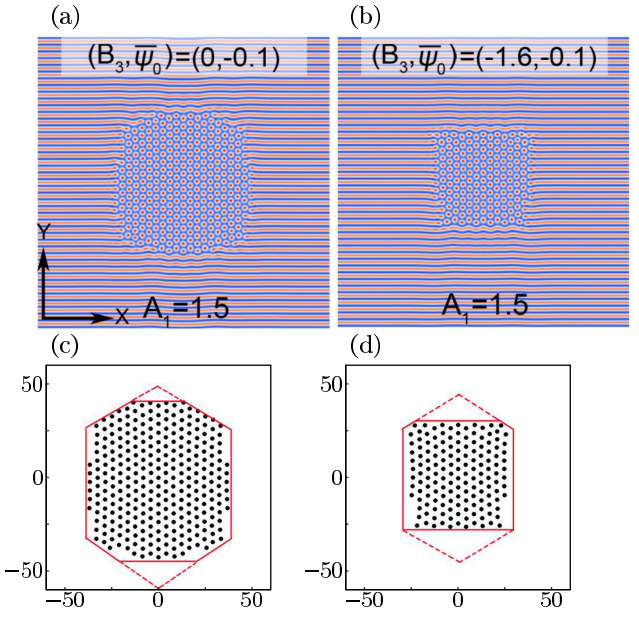

FIG. 3. (Color online) The PTC shape in the CSA phase for $A_1 = 1.5$ and (a) and (c) $B_3 = 0$ and (b) and (d) $B_3 = -1.6$, where the close-packed crystal direction is perpendicular to the stripe in the CSA phase. (c) and (d) show a sketch of the PTC shape in the CSA phase. The red dashed lines visualize the extrapolation to a hexagonal shape.

B. Topological defect formation

The PTC phase exhibits not only the characteristics of the crystalline phase but also nematic ordering with topological defects. Here we examine how the nematic ordering evolves at the PTC-isotropic and the PTC-CSA interfaces. The simulations are set up as above. But we restrict ourselves to the interface in the regime of constant growth velocity. Figure 4 shows the nematic order parameter $S(\vec{r})$ and director $\hat{n}(\vec{r})$ at the [12] interface. In the PTC phase along the shown direction, $+1$ vortices and pairs of $-\frac{1}{2}$ disclinations alternate [24].

Towards the isotropic phase, not only does the nematic order parameter decrease, but also the structure of the ordering changes [see Figs. 4(a) and 4(c) and details in Fig. 5]. The $+1$ vortex splits into two $+\frac{1}{2}$ disclinations. This disclination pair increases its distance and finally vanishes as the nematic ordering vanishes. Growth towards the CSA phase changes the situation only a little [Figs. 4(b) and 4(d)]. The PTC and CSA phases show different nematic ordering, but the splitting of $+1$ vortices is also observed. Furthermore, in the PTC isotropic growth the nematic order parameter forms a weak columnar structure ahead of the growth front. Thus, the PTC isotropic phase transition has an intermediate stripe phase. The structure of the topological defects of the nematic director $\hat{n}(\vec{r},t)$ at the PTC growth front are similar for both cases.

Figure 5 shows the formation process of the topological defect structure of the PTC phase grown towards the CSA

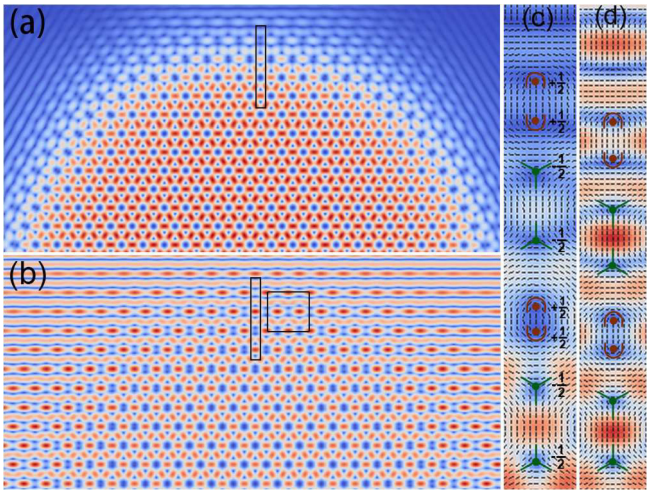

FIG. 4. (Color online) The topological structure of the PTC phase grown from (a) the isotropic phase and (b) the CSA phase. A magnified view of the area denoted by black boxes in (a) and (b) is given in (c) and (d), respectively, where the short dashes represent the director field of the topological structure.

phase. First, fluctuation in the $\hat{n}(\vec{r},t)$ field and nematic order parameter field $S(\vec{r},t)$ arises at the PTC growth front. This leads to $+\frac{1}{2}$ and $-\frac{1}{2}$ disclination pairs [Figs. 5(a) and 5(b)]. Next, two $+\frac{1}{2}$ disclinations approach each other gradually and coalesce into a $+1$ vortex [Figs. 5(c) and 5(e)]. The $-\frac{1}{2}$ disclinations do not move. At the end, a basic unit, the $+1$ vortex surrounded by six $-\frac{1}{2}$ disclinations, is formed [Fig. 5(f)]. This constitutes the topological defect structure in the bulk PTC phase. It was found that the coalescence of two disclinations with the same charge is energetically unfavored [34]. Nevertheless, during PTC growth, the advancing interface drives coalescence of two $+\frac{1}{2}$ disclinations. In the following, the kinetics of this topological defect formation will be discussed in more detail.

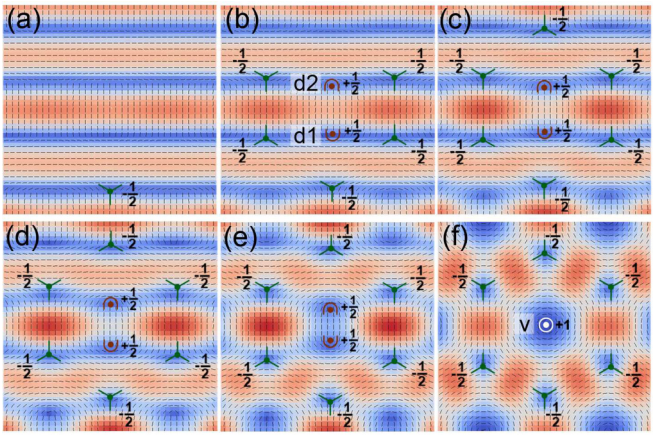

FIG. 5. (Color online) Snapshots of the topological defect structure formation in the region enclosed by the square box in Fig. 4(b) during the PTC growth in the CSA phase. Here d1 and d2 are a pair of $+\frac{1}{2}$ disclinations. The PTC-CSA interface moves from bottom to top from (a) to (f), and for (d) and (e) the region around d1 and d2 is located inside the PTC-CSA interface.

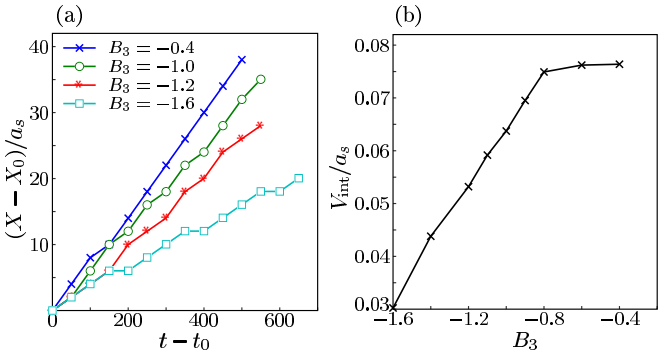

FIG. 6. (Color online) The growth kinetics of the PTC-CSA interface. The displacement of PTC-CSA interface vs (a) time t and (b) growth velocity for various B_3. X is the position of the PTC-CSA interface at different times, and X_0 is the initial position at time t_0.

First, we study the growth velocity of the PTC nucleus from the CSA phase along the direction normal to stripes, as shown in Fig. 4(b). After some initial relaxation, the displacement of the PTC-CSA interface increases linearly with time, and a constant growth velocity $V_{\rm int}$ is achieved [Fig. 6(a)]. The dependence of the growth velocity on the coupling strength B_3 is shown in Fig. 6(b). Strong and weak coupling regimes can be identified. For strong coupling, the growth velocity increases linearly with B_3, changing from -1.6 to -0.8. For weak coupling, when B_3 is in the range between -0.8 and -0.4, the growth velocity shows little dependence on B_3. Starting from the growth velocity $V_{\rm int}$, the defect moving velocity V_d is scaled as $\widetilde{V} = V_d/V_{\rm int}$, and time t is scaled as $\widetilde{t} = t/(a_s/V_{\rm int})$, with the lattice constant of the CSA phase $a_s = 2\pi/\sqrt{1/2} \approx 8.8858$. This can be used to count the number of lattices in the CSA phase that the PTC-CSA interface has advanced.

The coalescence of two $+\frac{1}{2}$ disclinations is illustrated in Fig. 7 in more detail. The positions of the topological defects are easily identified at the minima of the nematic order parameter $S(\vec{r})$ [Fig. 7(a)]. Initially, there are two minima in $S(\vec{r},t)$ profiles which correspond to disclinations d1 and d2, respectively. The two minima approach gradually and coalesce finally at $\widetilde{t} \approx 19.1$. To compare the evolution of the density field and the orientational field, we extract the density profile when the PTC-CSA interface is sweeping the region around d1 and d2 at $\widetilde{t} = 9.95$. As shown in Fig. 7(b), the peak value of the density profile at the position marked by the left vertical dotted line almost equals that of the bulk PTC phase. However, the corresponding $S(\vec{r},t)$ profile at the same time ($\widetilde{t} = 9.95$) indicates that the evolution of the orientational field in the region around d1 and d2 is still far from being complete. The distance between d1 and d2 versus $\widetilde{t}$ is illustrated in Fig. 7(c). We can see that d1 and d2 move nearly symmetrically. The velocities of d1 and d2 are given in Fig. 7(d). The largest velocity occurs about the time $\widetilde{t} = 9.95$. This corresponds to the moment when the growth front is sweeping the region around d1 and d2, which corresponds to the state in Fig. 5(e), and when the density field evolution around d1 and d2 is almost complete, as shown in Fig. 7(b). As the PTC-CSA interface approaches the region around d1 and d2, the velocities of d1 and d2 increase rapidly, while they decrease steeply after the interface moves past them. In other words, the evolution of

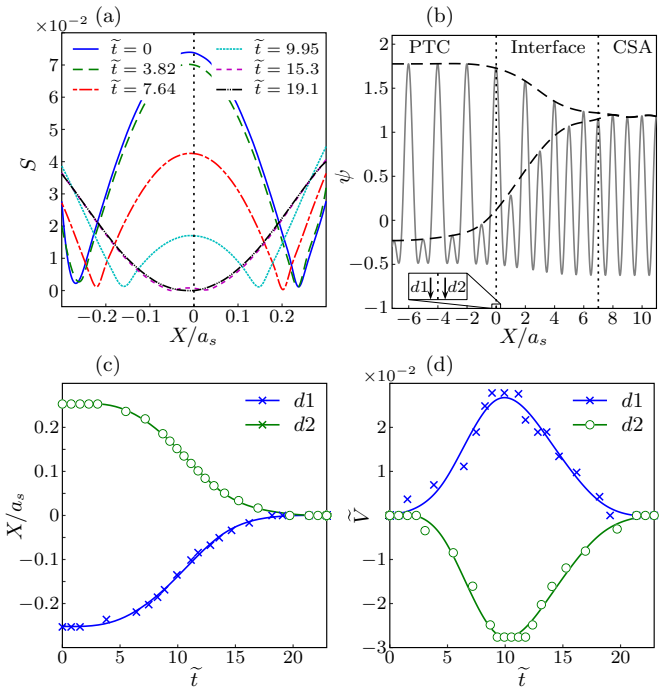

FIG. 7. (Color online) The moving trajectory of two $+\frac{1}{2}$ disclinations, d1 and d2, corresponding to Fig. 5, as represented by (a) the $S(\vec{r},t)$ profile and (b) the profile of the density field corresponding to time $t = 130$ (i.e., $\widetilde{t} = 9.95$), and (c) the position and (d) the velocity of d1 and d2. The region between the two vertical dotted lines in (b) indicates the PTC-CSA interface (the left and the right boundaries of the interface are determined by the criterion that the height of the peaks is lower than 0.95 of that in the bulk PTC phase and the CSA phase, respectively). The inset in (b) is a zoom of the X interval as in (a), with the arrows indicating the position of the d1 and d2 defects at time $\widetilde{t} = 9.95$.

topological defect formation is accelerated by the advancing PTC-CSA interface. When the $+1$ vortex forms through the coalescence of d1 and d2, the interface has moved forward by a distance of about 20 lattice constants from the position when it passes d1 and d2.

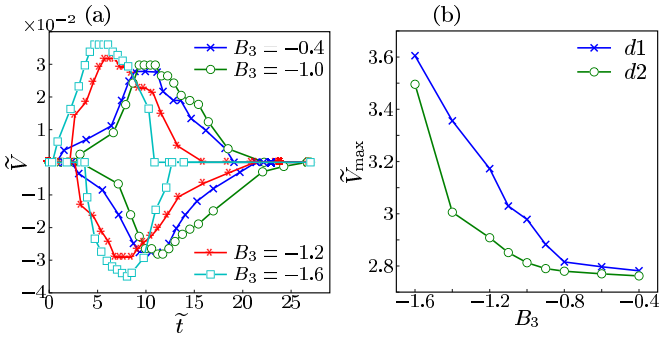

FIG. 8. (Color online) The influences of coupling strength B_3 on topological defects formation kinetics: (a) the velocity of two $+\frac{1}{2}$ disclinations during the formation of $+1$ vortex for various B_3 and (b) the peak value of the velocity curves as shown in (a) as a function of B_3.

Finally, we investigate the influence of coupling strength on $+1$ vortex formation kinetics. As shown in Fig. 8(a), with coupling strength increasing by decreasing B_3 from -0.4 to -1.6, the peaks of the velocity curves increase, and the scaled time $\widetilde{t}$ needed for the formation of a $+1$ vortex decreases. This indicates that the evolution from d1 and d2 to a $+1$ vortex can be completed faster for higher coupling strength. The dependence of peak velocities of the curves in Fig. 8(a) on B_3 is summarized in Fig. 8(b). For weak coupling strength when B_3 is between -0.8 and -0.4, the peak velocities of d1 and d2 are nearly the same, and the motions of d1 and d2 are approximately symmetrical. However, with coupling strength increasing further ($B_3 < -1.0$), the peak velocities of d1 and d2 increase substantially, and d1, the disclination moving along the same direction as the PTC-CSA interface, has a larger peak velocity than that of d2, which moves opposite to the PTC-CSA interface. Thus, it is shown that the increase in coupling strength accelerates the topological defect formation during PTC growth.

IV. CONCLUSION

In summary, by using the LC-PFC model we investigated the growth of PTC nucleus from the isotropic phase and the CSA phase on particle scale. An overall picture for the growth of the PTC phase was presented for shape evolution and nematic topological defect structure formation. It was demonstrated that the shape evolution for the PTC phase growth is mainly determined by crystalline anisotropy. The coupling strength exerts little influence on the shape of growing PTC nucleus. Only the shape of the PTC nucleus grown from the CSA phase also depends on the misorientation of PTC and CSA. Moreover, for the formation process of the nematic topological structure of the PTC phase, the formation of the PTC topological structure starts from nucleation of $+\frac{1}{2}$ and $-\frac{1}{2}$ disclination pairs at the PTC growth front and leads to the coalescence of $+\frac{1}{2}$ pairs forming a hexagonal cell consisting of one $+1$ vortex surrounded by six $-\frac{1}{2}$ disclinations. The coupling strength influences the kinetics of topological defect formation, and strong coupling strength accelerates the formation of nematic topological structure. Thus, while morphological shapes of plastic crystals might look similar to that of metal systems, the dynamics of the growth process shows strong differences.

Experiments with two-dimensional confined colloids could be done in order to verify our findings. Colloidal suspensions may be confined on two-dimensional substrates, and the positional and orientational ordering may be measured directly [5,35]. In order to analyze defect formation a time dependent measurement is not necessary, as the defect structure around an interface already resamples the evolution of the single defects. Thus, it would be sufficient to focus on the interface (see Fig. 4).

For future work, it would be interesting and meaningful to extend the present study to three spatial dimensions. The topological defect formation of a plastic crystal with crystal structures, such as simple cubic, body-centered crystal, face-centered crystal, etc., may provide more amazing scenarios of topological defect formation. Also, it would be worth studying the plastic crystal growth with polar and nonspherical particles.

ACKNOWLEDGMENTS

This work has been supported by EU FP7, PHASEFIELD under Grant No. 247504, Deutsche Forschungsgemeinschaft (DFG) within SPP1296 (Grant No. Vo899/7), the Nature Science Foundation of China (Grants No. 10974228 and No. 51071128), and a 2013 Sino-German (CSC-DAAD) postdoctoral scholarship program.

APPENDIX: SEMI-IMPLICIT FOURIER METHOD FOR THE LC-PFC MODEL

A system of six coupled nonlinear partial differential equations needs to be solved in the liquid crystal PFC model. In order to numerically solve this system efficiently, we decoupled and linearized it. Considering the tracelessness and symmetry of the nematic tensor as shown in Eq. (1), we can extract the variables $q_i \equiv Q_{i,1}$ and $q_i^\natural \equiv Q_{i,1}^\natural$, with $\mathbf{q} = (q_1,q_2)^\top$ and $\mathbf{q}^\natural = (q_1^\natural,q_2^\natural)^\top$. The dynamic equations (3) and (4) thus have the compact form

$$\begin{aligned}\dot{\psi} &= 2\alpha_1 \Delta\psi^\natural + 2\alpha_3 \blacktriangle_i q_i^\natural,\\ \dot{q}_i &= 4\alpha_1 \Delta q_i^\natural - 8\alpha_4 q_i^\natural + 2\alpha_3 \blacktriangle_i \psi^\natural.\end{aligned} \tag{A1}$$

The terms containing the operator $\blacktriangle$ can be expanded as

$$\blacktriangle_i q_i^\natural = (\partial_1\partial_1 - \partial_2\partial_2)q_1^\natural + 2\partial_1\partial_2 q_2^\natural,$$

and the thermodynamic conjugates read

$$\begin{aligned}\psi^\natural &= \omega_\psi(\psi,\mathbf{q}) + \overbrace{2A_1\psi + 2A_2(\Delta+\Delta^2)\psi}^{L_\psi^\psi(\psi)} + \overbrace{(-B_3)\blacktriangle_i q_i}^{L_\psi^q(\mathbf{q})},\\ q_i^\natural &= \omega_q(\psi,\mathbf{q})_i + \underbrace{4D_1 q_i - 2D_2\Delta q_i}_{L_q^q(q_i)} + \underbrace{(-B_3)\blacktriangle_i\psi}_{L_{q,i}^\psi(\psi)},\end{aligned} \tag{A2}$$

with the linear parts $L_\psi^\psi(\psi), L_\psi^q(\mathbf{q}), L_q^q(q_i)$, and $L_{q,i}^\psi(\psi)$ and the polynomials

$$\begin{aligned}\omega_\psi(\psi,\mathbf{q}) &= -\psi^2 + \tfrac{2}{3}\psi^3 + \tfrac{1}{2}(2\psi-1)\left(q_1^2+q_2^2\right),\\ \omega_q(\psi,\mathbf{q})_i &= \psi(\psi-1)q_i + \tfrac{1}{4}q_i\left(q_1^2+q_2^2\right).\end{aligned} \tag{A3}$$

We define the Fourier wave vector $\mathbf{k} = (k_1,k_2)^\top$ and introduce the Fourier transform $\mathcal{F}$ of the order parameter fields as

$$\psi \mapsto \mathcal{F}(\psi) =: \hat{\psi}(\mathbf{k}), \quad q_i \mapsto \mathcal{F}(q_i) =: \hat{q}_i(\mathbf{k}).$$

Thus, we can write the differential operators in Fourier space as

$$\begin{aligned}\Delta \to \hat{\Delta} &:= -\left(k_1^2+k_2^2\right) = -|\mathbf{k}|^2,\\ \blacktriangle \to \hat{\blacktriangle} &:= \begin{pmatrix} -\left(k_1^2-k_2^2\right)\\ -k_1k_2\end{pmatrix}.\end{aligned} \tag{A4}$$

Discretizing (A1) in time using a semi-implicit backward Euler discretization and transforming the equation to Fourier space lead to the spectral method used in our calculations. Therefore, we transform the linear differential operators L_*^* of (A2) using the operators defined above and denote them with a hat, i.e.,

$$\begin{aligned}\hat{L}_\psi^\psi[\hat{\psi}] &:= 2A_1\hat{\psi} + 2A_2(\hat{\Delta}+\hat{\Delta}^2)\hat{\psi}\\ &= [2A_1 + 2A_2(-|\mathbf{k}|^2 + |\mathbf{k}|^4)]\hat{\psi},\end{aligned} \tag{A5}$$

and the other operators are transformed in an analogous manner.

The nonlinear polynomials (A3) are evaluated in real space and transformed afterwards, i.e.,

$$\hat{\omega}_\psi(\psi,\mathbf{q}) := \mathcal{F}(\omega_\psi(\psi,\mathbf{q})). \tag{A6}$$

Therefore, in each time step the order parameters ψ and $\mathbf{q}$ have to be transformed between real and Fourier spaces using efficient implementations of $\mathcal{F}$ and $\mathcal{F}^{-1}$.

Let $0 = t^0 < t^1 < \cdots < t^N = T$ be a discretization of a time interval $[0,T]$, with $t^{n+1} - t^n =: \tau$ being the time step width. The finite difference approximation

$$\dot{\hat{\psi}} \approx \frac{\hat{\psi}^{n+1} - \hat{\psi}^n}{\tau},$$

with $\hat{\psi}^n \equiv \hat{\psi}(t^n)$ and $\dot{\hat{q}}_i$ being calculated in an analogous manner, inserted into the transformed equations, using (A5) and (A6), leads to an iterative procedure: Let $\hat{\psi}^0 = \mathcal{F}(\psi^0)$, $\hat{\mathbf{q}}^0 = \mathcal{F}(\mathbf{q}^0)$.

For $n = 0,1,2,\ldots,N$

(1) Solve

$$\begin{aligned}&\left(1 - \tau\left[2\alpha_1\hat{\Delta}\hat{L}_\psi^\psi + 2\alpha_3\hat{\blacktriangle}_i\hat{L}_{q,i}^\psi\right]\right)\hat{\psi}^{n+1}\\ &\quad= \Big(\hat{\psi}^n + \tau\Big[2\alpha_1\hat{\Delta}\left\{\hat{L}_\psi^q[\hat{\mathbf{q}}^n] + \hat{\omega}_\psi(\psi^n,\mathbf{q}^n)\right\}\\ &\qquad + 2\alpha_3\hat{\blacktriangle}_i\left\{\hat{L}_q^q\left[\hat{q}_i^n\right] + \hat{\omega}_q(\psi^n,\mathbf{q}^n)_i\right\}\Big]\Big).\end{aligned} \tag{A7}$$

(2) Transform to real space:

$$\psi^{n+1} = \mathcal{F}^{-1}(\hat{\psi}^{n+1}).$$

(3) For $i = 1,2$, solve

$$\begin{aligned}&\left(1 - \tau\left[(4\alpha_1\hat{\Delta} - 8\alpha_4)\hat{L}_q^q\right]\right)\hat{q}_i^{n+1} - \tau 2\alpha_3\hat{\blacktriangle}_i\hat{L}_\psi^q\left[\hat{\mathbf{q}}_{(i)}^{n,n+1}\right]\\ &\quad= \Big(\hat{q}_i^n + \tau\Big[(4\alpha_1\hat{\Delta} - 8\alpha_4)\left\{\hat{L}_{q,i}^\psi[\hat{\psi}^{n+1}] + \hat{\omega}_q(\psi^{n+1},\mathbf{q}^n)_i\right\}\\ &\qquad + 2\alpha_3\hat{\blacktriangle}_i\left\{\hat{L}_\psi^\psi[\hat{\psi}^{n+1}] + \hat{\omega}_\psi(\psi^{n+1},\mathbf{q}^n)\right\}\Big]\Big),\end{aligned} \tag{A8}$$

where $\hat{\mathbf{q}}_{(i)}^{n,n+1}$ are intermediate vectors defined as

$$\hat{\mathbf{q}}_{(1)}^{n,n+1} := \begin{pmatrix}\hat{q}_1^{n+1}\\ \hat{q}_2^n\end{pmatrix}, \quad \hat{\mathbf{q}}_{(2)}^{n,n+1} := \begin{pmatrix}\hat{q}_1^n\\ \hat{q}_2^{n+1}\end{pmatrix}.$$

(4) Transform to real space:

$$q_i^{n+1} = \mathcal{F}^{-1}\left(\hat{q}_i^{n+1}\right),\ i = 1,2.$$

In Eq. (A8) the updated values ψ^{n+1} and $\hat{\psi}^{n+1}$ can be used.

[1] G. J. Vroege and H. N. W. Lekkerkerker, Rep. Prog. Phys. **55**, 1241 (1992).

[2] M. P. Taylor and J. Herzfeld, J. Phys.: Condens. Matter **5**, 2651 (1993).

[3] P. Cremer, M. Marechal, and H. Löwen, Europhys. Lett. **99**, 38005 (2012).

[4] E. B. Mock and C. F. Zukoski, Langmuir **23**, 8760 (2007).

[5] A. F. Demirörs, P. M. Johnson, C. M. van Kats, A. V. Blaaderen, and A. Imhof, Langmuir **26**, 14466 (2010).
[6] I. D. Hosein, B. S. John, S. H. Lee, F. A. Escobedo, and C. M. Liddell, J. Mater. Chem. **19**, 344 (2009).
[7] R. Rey, J. Phys. Chem. B **112**, 344 (2008).
[8] A. V. Tkachenko and Y. Rabin, Phys. Rev. E **55**, 778 (1997).
[9] M. Roth and R. D. Etters, Phys. Rev. B **44**, 6581 (1991).
[10] M. J. Bowick and L. Giomi, Adv. Phys. **58**, 449 (2009).
[11] S. J. Gerbode, U. Agarwal, D. C. Ong, C. M. Liddell, F. Escobedo, and I. Cohen, Phys. Rev. Lett. **105**, 078301 (2010).
[12] H. Löwen, Phys. Rep. **237**, 249 (1994).
[13] S. Dhakal, F. J. Solis, and M. Olvera de la Cruz, Phys. Rev. E **86**, 011709 (2012).
[14] K. R. Elder, M. Katakowski, M. Haataja, and M. Grant, Phys. Rev. Lett. **88**, 245701 (2002).
[15] K. R. Elder and M. Grant, Phys. Rev. E **70**, 051605 (2004).
[16] H. Emmerich, H. Löwen, R. Wittkowski, T. Gruhn, G. I. Tóth, G. Tegze, and L. Gránásy, Adv. Phys. **61**, 665 (2012).
[17] G. Tegze, L. Gránásy, G. I. Tóth, J. F. Douglas, and T. Pusztai, Soft Matter **7**, 1789 (2011).
[18] S. Tang, Z. J. Wang, Y. L. Guo, J. C. Wang, Y. M. Yu, and Y. H. Zhou, Acta Mater. **60**, 5501 (2012).
[19] S. Tang, R. Backofen, J. Wang, Y. Zhou, A. Voigt, and Y. M. Yu, J. Cryst. Growth **334**, 146 (2011).
[20] Y. M. Yu, R. Backofen, and A.Voigt, J. Cryst. Growth **318**, 18 (2011).
[21] In the case of polar liquid crystals an additional field, the local polarization $\vec{P}$, is introduced; see, e.g., [31,32].
[22] H. Löwen, J. Phys.: Condens. Matter **22**, 364105 (2010).
[23] R. Wittkowski, H. Löwen, and H. R. Brand, Phys. Rev. E **82**, 031708 (2010).
[24] C. V. Achim, R. Wittkowski, and H. Löwen, Phys. Rev. E **83**, 061712 (2011).
[25] S. Praetorius, A. Voigt, R. Wittkowski, and H. Löwen, Phys. Rev. E **87**, 052406 (2013).
[26] E. R. Rubinstein and M. E. Glicksman, J. Cryst. Growth **112**, 84 (1991).
[27] P. Oswald and P. Pieranski, *Smectic and Columnar Liquid Crystals* (Taylor and Francis, New York, 2006).
[28] N. D. Mermin, Rev. Mod. Phys. **51**, 591 (1979).
[29] G. P. Alexander, B. G. Chen, E. A. Matsumoto, and R. D. Kamien, Rev. Mod. Phys. **84**, 497 (2012).
[30] R. Backofen and A. Voigt, J. Phys.: Condens. Matter **21**, 464109 (2009).
[31] R. Wittkowski, H. Löwen, and H. R. Brand, Phys. Rev. E **83**, 061706 (2011).
[32] R. Wittkowski, H. Löwen, and H. R. Brand, Phys. Rev. E **84**, 041708 (2011).
[33] S. V. Khare, S. Kodambaka, D. D. Johnson, I. Petrov, and J. E. Greene, Surf. Sci. **522**, 75 (2003).
[34] T. Lopez-Leon, M. A. Bates, and A. Fernandez-Nieves, Phys. Rev. E **86**, 030702(R) (2012).
[35] M. Brunner and C. Bechinger, Phys. Rev. Lett. **88**, 248302 (2002).